01 Oct 2022

Enabling Ultrathick Electrodes Via a Microcasting Process for High Energy and Power Density Lithium-Ion Batteries

Tazdik Patwary Plateau

Hiep Pham

Yaqi Zhu

Ming-Chuan Leu
Missouri University of Science and Technology, mleu@mst.edu

et. al. For a complete list of authors, see https://scholarsmine.mst.edu/mec_aereng_facwork/4924

Recommended Citation

T. P. Plateau et al., "Enabling Ultrathick Electrodes Via a Microcasting Process for High Energy and Power Density Lithium-Ion Batteries," *Advanced Energy Materials*, vol. 12, no. 38, article no. 2201353, Wiley; Wiley-VCH Verlag, Oct 2022.
The definitive version is available at https://doi.org/10.1002/aenm.202201353

ADVANCED ENERGY MATERIALS
www.advenergymat.de

Enabling Ultrathick Electrodes via a Microcasting Process for High Energy and Power Density Lithium-Ion Batteries

*Tazdik Patwary Plateau, Hiep Pham, Yaqi Zhu, Ming Leu, and Jonghyun Park**

Thickening electrodes is one effective approach to increase active material content for higher energy and low-cost lithium-ion batteries, but limits in charge transport and huge mechanical stress generation result in poor performance and eventual cell failure. This paper reports a new electrode fabrication process, referred to as μ-casting, enabling ultrathick electrodes that address the trade-off between specific capacity and areal/volumetric capacity. The proposed μ-casting is based on a patterned blade, enabling facile fabrication of 3D electrode structures. The study reveals the governing properties of μ-casted ultrathick electrodes and how this simultaneously improves battery energy/power performance. The process facilitates a short diffusion path structure that minimizes intercalation-induced stress, improving energy density and cell stability. This work also investigates the issues with structural integrity, porosity, and paste rheology, and also analyzes mechanical properties due to external force. The μ-casting enables an ultrathick electrode (≈280 μm) that more effectively utilizes NMC-811 ($LiNi_{0.8}Mn_{0.1}Co_{0.1}O_2$) cathode and mesocarbon microbeads anode active materials compared to conventional thick electrodes, allowing high-mass loading (35.7 mg cm^{-2}), 40% higher specific capacity, and 30% higher areal capacity after 200 cycles, high C-rate performance, and longer cycle life.

1. Introduction

For modern portable electronic devices and electric vehicles, it is necessary to increase the performance of lithium-ion batteries (LIBs) to achieve high energy and power density.[1–4] Though numerous new materials have been introduced, the performance depends not only on battery material but also on the structure of the electrodes, where the optimization of the battery architecture is critical.[4–6] In LIB performance studies, one of the most common metrics is the gravimetric capacity or the specific capacity (mAh g^{-1}) of the electrode materials. However, only having a high specific capacity is not sufficient to meet the battery performance needs since the total energy and power are also limited by area and volume. Eventually, an increase in the energy and power can be made by increasing the amount of the active materials in the electrodes via thick or compacted electrodes, and is typically referred to as high mass loading. Despite this, increasing the mass loading of electrodes has substantial limitations. First, the transport of lithium ions and electrons through the entire electrode is hindered due to the creation of long paths for Li^+ ion transport.[7] Second, a high amount of active materials used in a thick electrode causes a reduction in the mechanical stability of the electrode due to increased internal stress generation during cycling.[1,5] Thus, careful design through innovative and facile fabrication techniques for LIB electrodes is required to meet the future energy demands.[7,8]

Conventionally, battery electrodes are fabricated by the tape casting method,[9–11] where a mixture of active materials, conducting materials, and binders are cast onto a current collector yielding a planer laminated composite structure. In this method, the key factors for increasing both areal capacity (mAh cm^{-2}) and active material utilization are electrode thickness, mass, and porosity. Particularly, forming a thick electrode is a straightforward approach to maximize use of active materials and minimize inactive material amounts to enhance battery energy density.[12–14] As mentioned, however, increasing the thickness of a battery electrode by using high active material loading faces significant challenges including: a compromise between energy density and power; large limitations in ionic transport due to long diffusion pathways (LDP); and poor mechanical stability. One work reported a 600 μm thick hybrid NMC-811 cathode mixed with solid-state electrolyte material was reported, where the total thickness was the sum of cathode and solid electrolyte thickness and only 30% solid loading of the NMC-811 active material was in the total hybrid structure of the electrode.[12] In another work, an ultrathick electrode (500 μm) was developed via a freeze-drying method, where a gum binder was mixed with single walled carbon nanotubes to improve contact between the active materials (NMC-811, $LiNi_{0.8}Mn_{0.1}Co_{0.1}O_2$), and a high mass loading of 511 mg cm^{-2} and areal capacity of 79.3 mAh cm^{-2} could be achieved. However, the cells showed huge degradation from the first cycle and the cells failed in 15 cycles. Furthermore, at a low mass loading the areal capacity decreased significantly, indicating that a higher total capacity was made by increasing

T. P. Plateau, H. Pham, Y. Zhu, M. Leu, J. Park
Department of Mechanical Engineering
Missouri University of Science and Technology
Rolla, MO 65409, USA
E-mail: parkjonghy@mst.edu

The ORCID identification number(s) for the author(s) of this article can be found under https://doi.org/10.1002/aenm.202201353.

DOI: 10.1002/aenm.202201353

the electrode mass at a fixed area.[11] Therefore, it is necessary to form a thick electrode having a high amount of active material while maintaining good cyclability. A prospective approach to utilize higher active material amounts is by implementing 3D geometries, which can facilitate the formation of a short diffusion path (SDP). An SDP geometry is defined by the presence of short, relatively straight, and nonwinding diffusion paths, which promotes fast ion transport and enhanced electrochemical reaction sites through a higher interfacial area between the anode and cathode.[1,7,8,14–17] Three-dimensionally structured SDP electrode designs have opened a new horizon for achieving improved LIB performance by enhancing ion transport and several approaches have been observed to make SDP electrodes at the microscale, which is related to the pore structure that is in turn affected by active particle shapes and orientation, and the macroscale, which relates to the homogeneity of local porosity.[3,7,8,14–16]

Recently, large improvements in the formation of 3D electrode architectures have been made by advanced manufacturing techniques such as aerosol jet printing and extrusion-based 3D printing techniques, which have garnered popularity due to flexible processing that can easily produce complex geometric designs with a wide selection of materials.[18–24] The aerosol jet printing technique has permitted the controlled formation of complex architecture electrodes based on silver metal.[20] However, the interdigitation between the complex shaped electrodes cannot be well achieved due to the technique's sensitivity to its manufacturing parameters, such as jet pressure and subsequent aerosol flow. On the other hand, electrodes formed through the extrusion-based printing have shown to offer marked improvement in battery performance,[25–27] where a novel hybrid 3D structured with SDP electrode was developed and was able to overcome the limitations of conventional laminated composite LDP electrodes. A high interfacial area could be formed by utilizing the 3D structured electrode, and allowed facile ion diffusion via a high contacting area and shortened ion diffusion path to achieve higher power (2.3 mW cm^{-2}) and energy density (64.6 J cm^{-2}) as compared to the conventional laminated electrode structure.[15,16] Different thick electrodes (600 µm) have been developed using higher amounts of nonconductive and nonactive materials to withstand the architecture, which can enhance the areal capacity by sacrificing 70–90% of their specific capacity due to poor contact between the active materials and long Li^+ ion diffusion path.[9,15,18,29–38] While many additive manufacturing techniques have been applied in the fabrication of 3D battery structures, the majority of these works are focused on developing microbatteries and few works consider the impact of the processing on active particle percolation and the resulting pore structure. Furthermore, traditional 3D printing-based battery manufacturing technologies face efficiency challenges related to their time-consuming, complicated, and costly fabrication process.[13]

Herein, a new process is proposed for the fabrication of SDP 3D structured LIB electrodes, which is called a 3D microcasting (µ-casting) process (US10804524B2).[27] In this approach, a 3D patterned doctor blade is introduced to prepare ultrathick 3D structured electrodes through tape casting, foregoing the complicated and time-consuming processes of conventional advanced manufacturing techniques to create a 3D geometry. In this process, a conventional doctor-blade is first used to make a planer base, and then the proposed µ-casting is conducted with a patterned 3D doctor blade to form a 3D patterned geometry from the planar base. The proposed µ-casted structured electrodes presents four vital battery performance advantages: 1) boosted active materials utilization by the formation of SDPs, which reduced distances between anode particles and cathode particles to achieve higher power performance by enhanced transport of electrons and ions; 2) enablement of ultrathick electrodes, which could achieve up to five times higher mass loading than conventionally fabricated electrodes, permitting both high specific and areal capacity without compromise; 3) sufficient structural integrity between the 3D structured anode and cathode to fabricate a interdigitated design between LIB components; and 4) low-cost manufacturing setup and exceedingly facile processing compared to the current technologies for making 3D electrode structures. In this work, ultrathick NMC-811 ($LiNi_{0.8}Mn_{0.1}Co_{0.1}O_2$) cathodes and mesocarbon microbeads (MCMB) anodes (≈280 µm thick and 35.73 mg cm^{-2}) could be successfully fabricated and were compared with the conventional laminated structured battery electrodes (5–12 mg; 3.25–7.8 mg cm^{-2} for anode and cathode). Conventionally a higher specific capacity is achieved by manufacturing thin electrodes.[37,39] The impact of the casting paste properties (paste viscosity and shear stress) with the resulting electrode's structural integrity was studied by considering the ratios of the paste constituent materials, where the paste properties were then optimized. The paste properties were also used to control the porosity and to establish mechanical structural integrity and strength utilizing the SDP structure. The interdigitated array of the 3D anode and cathode was then investigated in terms of feature shape postdrying and the resulting interface between the cathode, anode, and separator. The mechanical strength of the electrode assembly was measured by applying external load to understand the strength of the µ-casted electrode. Moreover, the mechanical degradation can happen due to long term cycling of the electrodes by stress generation and so it was also evaluated after long term cycling, where µ-casted electrodes showed less defect formation than the conventional laminated electrodes. To understand the stress generation in individual particles and its correlation to the electrode level behavior, a modeling study was conducted by coupling the analyses of the microscale stress and macroscale stress from the Li^+ ion particle level to the µ-casted electrode level. The simulation results support the mechanical degradation results, where the stress generation in the µ-casted electrode was mitigated compared to the conventional laminated structured electrode.

2. Results and Discussion

The SDP structure design facilitates the ionic movement in the electrodes, allowing for more active material utilization in the developed µ-casting process enables ultrathick electrodes. For this, a patterned doctor blade (**Figure 1**a) is manufactured via electrical discharge machining (EDM). The overall procedure for the µ-casting process is illustrated in Figure 1b and digital images of the µ-casting doctor blade, µ-casted anode, and µ-casted cathode are attached in Figure S6 of the Supporting

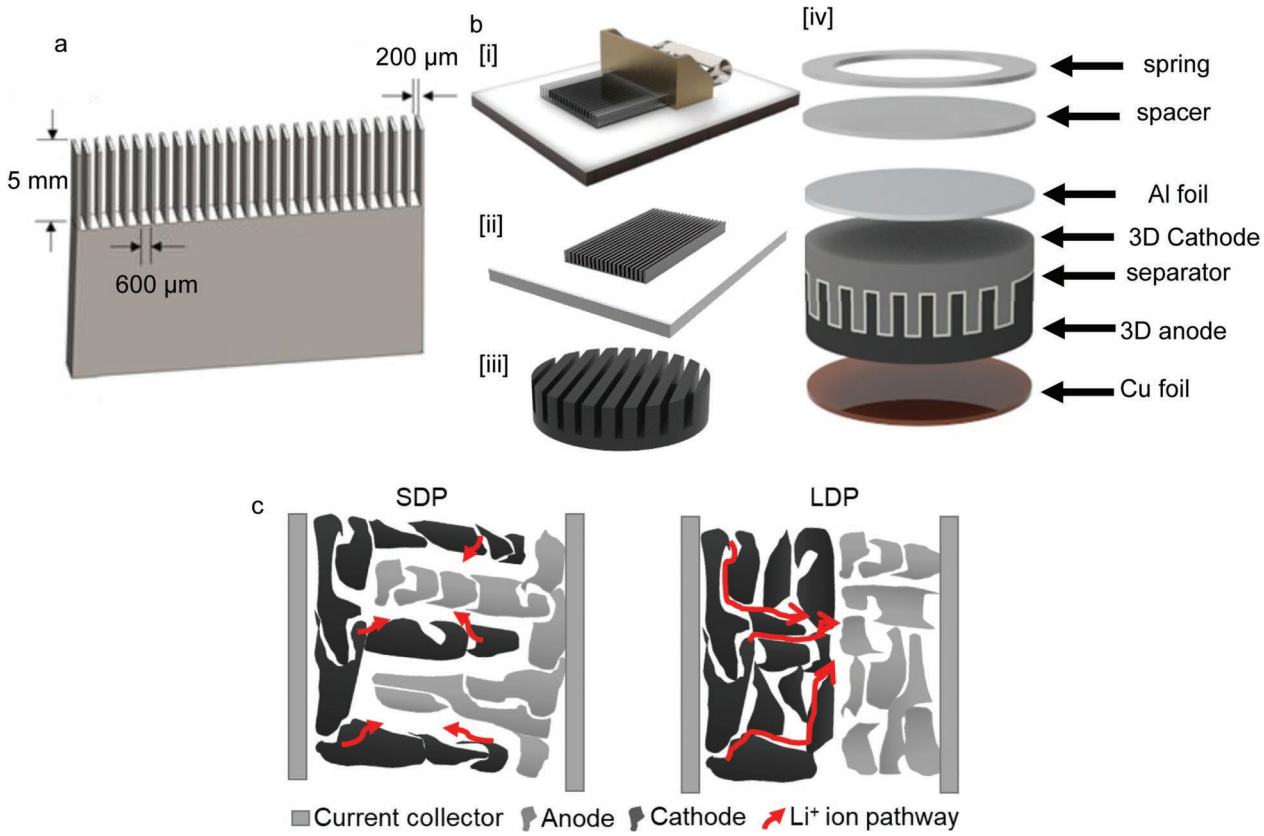

Figure 1. a) Schematic diagram of a patterned 3D doctor blade for μ-casting. b) μ-casting fabrication process to form ultrathick electrodes by using a conventional doctor-blade followed by 3D doctor blade (i), followed by drying and heating (ii), followed by cutting according to CR 2032 coin cell anode and cathode size (iii) and finally the coin cell-assembly of the battery (iv); and c) efficient utilization of the active materials by SDP structured thick electrodes compared to LDP structure thick electrodes due to shorter ion movement pathway.

Information. More details are described inthe Experimental Section.

Figure 1c shows schematic diagrams for a conventional casted structure with LDP and the proposed 3D design with SDP. The ion diffusion path determines the performance of the battery (such as specific capacity, areal capacity, etc.). A longer diffusion path creates a long travel path for lithium ions, which hinders the transfer of Li^+ ions and lowers the battery performance. Conventional electrodes are intentionally fabricated as thin layers (60 μm) to lower the ion diffusion path. Because the thick conventional simple flat structure creates a long travel distance for Li^+ ions between the anode and cathode, a high Li^+ concentration gradient is developed that consequently yields poor utilization of active materials. On the other hand, the SDP design enables shorter Li^+ ion diffusion pathways in ultrathick electrodes, permitting the maximum amount of the active materials to be utilized for both the anode and cathode. Moreover, thick conventional laminated electrodes have an increased presence of LDP and random paths which impedes ion transfer, limiting electrodes to very thin structures (3.25–7.8 mg cm^{-2}) to avoid performance losses as a result of poor ion transport.[37] Before going into the μ-casting process, the impact of the electrode thickness was investigated based on the electrodes with LDP designed conventional laminated structures using 8 CR2032 coin cells for each case (Figure S10, Supporting Information). Both types of cells were cycled for 20 cycles at 0.1 C and then 80 cycles at 0.5 C. As expected, the thick electrodes (140 μm) showed lower specific capacity than those from the thin electrode (60 μm). After 20 cycles at 0.1 C, the overall average capacity is 175 mAh g^{-1} for the thin electrodes and 155 mAh g^{-1} for thick electrodes, which align with the reported values.[14] As the C-rate increased to 0.5 C, the capacity became lower for both thin (155 mAh g^{-1}) and thick (132 mAh g^{-1}) electrodes and the thin electrode showed better performance (Figure S10, Supporting Information).

2.1. Paste Characteristics and Porosity

The electrode performance depends on its porosity, where an optimal porosity that yields the best electrochemical performance exists. In particular, calendaring is an important process in the battery manufacturing process and contributes significantly to the control of the electrode porosity. The electrodes become compacted during calendaring, which enhances the mechanical stability, controls the porosity of the electrode.[40] However, the porosity of an electrode evolves regardless of the calendaring process, where electrode drying postcasting

initiates the porosity growth and is dictated by the composition (material and solvent ratios) and paste properties of the electrode casting paste. To control porosity in the 3D structures via the μ-casting process, the paste composition and properties were considered with respect to the features to be retained after drying, including the impact of the solution solid loading (SL, volumetric ratio of solids in a solution). These qualities are all connected by two key physical properties of the casting paste: viscosity and shear stress, where those paste properties are important for the final porosity of the electrode and in obtaining a controlled 3D shape with good structural integrity.[11,24]

To establish the desired structure, it is very important to optimize the paste properties. By using higher solid loading, the paste viscosity and the shear stress were increased, which can maintain the integrity of the structured electrodes. In our previous work related to a similarly structured 3D electrode, a 30% SL showed the best performance than lower and higher SL%[14,33] and was initially considered for the μ-casting process but when used to fabricate electrodes using the μ-casting process, the structure could not be retained and collapsed. The SL was then increased to 40%, where the structure could then be maintained without collapse. Increasing the SL percentage more than 40% SL decreases the porosity of the electrode, which could result in low cycling performance,[14,33] and thus higher SL were not considered. To understand why a 30% SL could not maintain the structural integrity of the 3D μ-casting electrode whereas a 40% SL could, a rheological measurement (**Figure 2**a) of the paste was done to observe the standoff stress of different SL and it indicated that both pastes exhibited a shear-thinning behavior as the stress was decreased by increasing the shear rate. Among them, the 40% SL paste showed higher standoff shear stress and higher viscosity at higher shear rate than the 30% SL. As a result, the 40% SL paste had better structural strength to avoid collapsing and had the ability to maintain the μ-casted 3D architecture after the heating and drying process (patterned structure can be seen in Figure 2b), whereas the 30% SL could not maintain the 3D structure and collapsed during the heating process (no structure can be seen in Figure 2c). Furthermore, a trapezoidal shape was observed including curved corners on the structure shown in Figure 2b, which occurred when the solvent was evaporated during the heating process and the 3D architecture collapsed to a slight extent. It is notable that the structure could not be formed when a lower solid loading was used, shown in Figure 2c. Another main limitation of the thick electrode is delamination of the electrode from the current collector due to poor adhesion between the components. While prior works which pattern the current collector demonstrated the ability to improve adhesion, another more straightforward way is to optimize the rheology of the casting paste and the paste binder.[41,42] It should be stated that increasing the binder amount cannot improve the adhesion between the electrode and the current collector; instead, the higher density paste can create better bonding between the current collector and electrode.[41] The density of the 40% SL paste is 33.33% higher than the density of the 30% SL paste which allows the 40% SL paste to have better bonding between the current collector and the electrode.

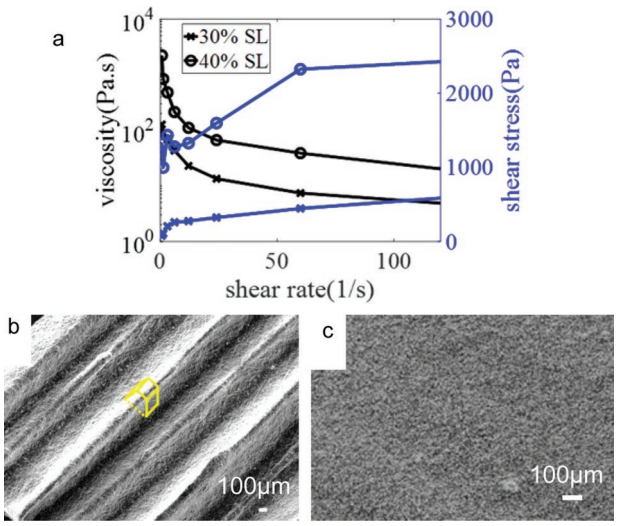

Figure 2. a) Paste viscosity and shear properties for the 30% and 40% solid loading (SL), b) the structure of the μ-casted electrode with 40% SL paste, and c) the structure of the μ-casted electrode with 30% SL paste.

The porosity of the anode and the cathode is a very important parameter for thick electrodes, where the best performance in terms of energy density was observed in our previous work at around 38% porosity for the cathode and 48% porosity for the anode.[33,43] A comparison of the porosities for the anode and cathode was made by considering 30% and 40% SL pastes. Our investigation showed that the 30% solid loading created a porosity of 0.6 and 40% SL created 0.497 porosity in the μ-casted anode electrode. For the conventional design of anode, the porosity was 0.492 for 40% SL. For the cathode the porosity of the μ-casted was 0.391 and the porosity of the conventional was 0.402. The porosity at 40% SL yielded the optimal value as found from our previous work, and, thus, a paste with 40% SL was then investigated for both the conventional tape casting process and μ-casting process.

2.2. Electrode Structures and Surface Morphology with Different Mass

The key to achieve higher areal capacity is to increase the mass loading, but the challenge is to not sacrifice the specific capacity caused by the ionic and electronic transport delay.[15,23] Here, a systematic study was conducted focusing on finding the relationship between the mass loading and capacity for 3D μ-casted electrodes and conventional laminated electrodes. The typical mass loading for coin cell formats ranges between 5 and 12 mg.[23] However, ultrathick 3D geometry with higher mass (25–55 mg) electrodes were compared to the conventional planar casted electrodes in this study. For the investigation, three different masses of the electrodes were grouped—Class A (25 to 35 mg), Class B (35 to 45 mg), and Class C (45 to 55 mg). After drying, the microstructures of the 3D structured ultrathick electrodes of all three Classes and the conventional structured electrodes were compared via a scanning electron microscopy (SEM) study.

Figure 3a–c shows the 3D structured electrodes for Class A, Class B, and Class C. The formed structure had a trapezoidal shape (marked in Figure 3a–c) including different heights for

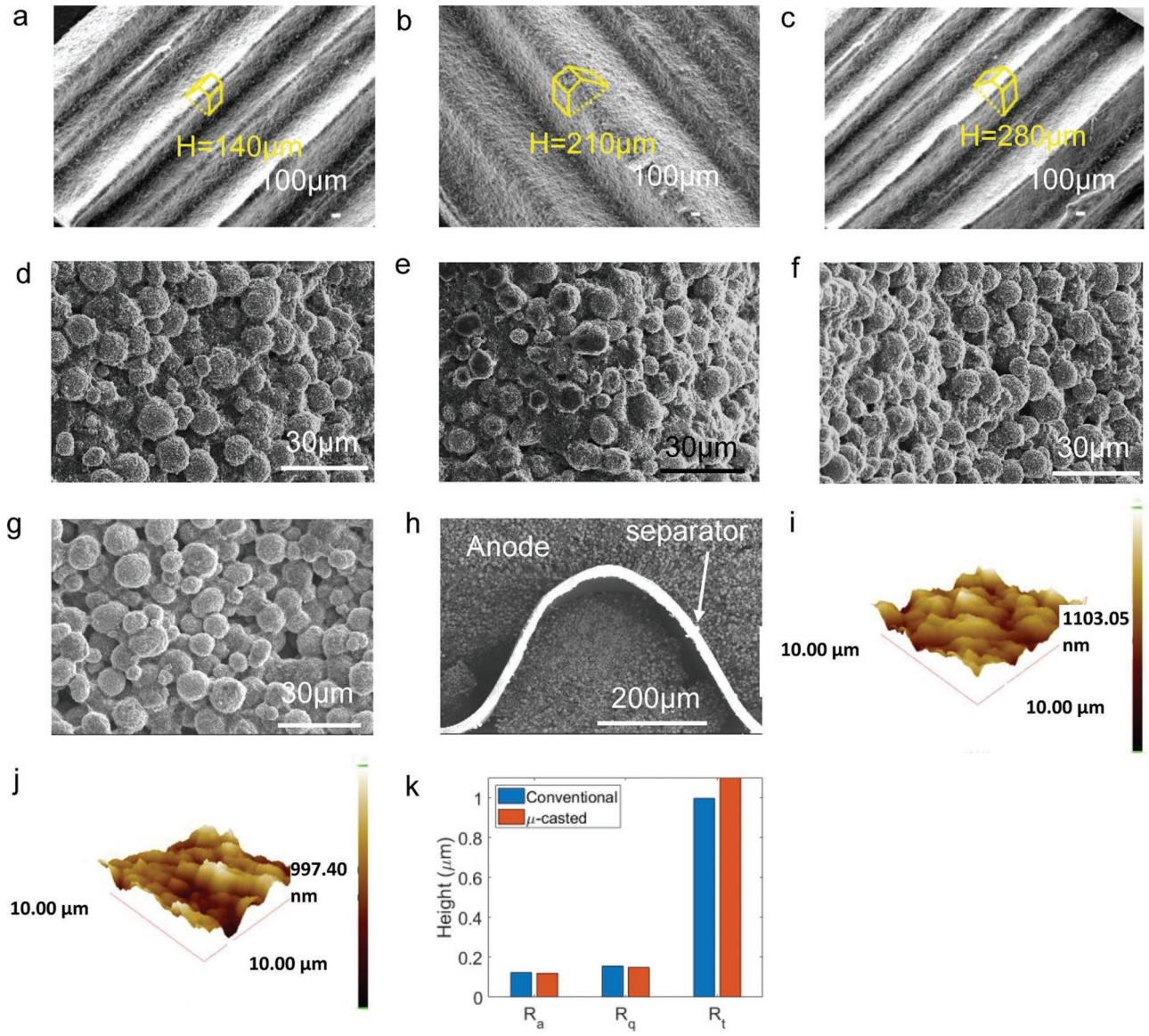

Figure 3. SEM images for μ-casted electrode of a) Class A, b) Class B, c) Class C (the trapezoidal box indicates the structure of the teeth, the dotted yellow line indicates the base line of the shape and *H* is the height of the structure). d) The μ-casted base layer, e) top layer of the μ-casted electrode, f) inclined edge of μ-casted electrode, and g) conventional laminated structure. h) The cross-sectional view of the attachment and placement between the μ-casted anode and cathode with the separator. i) AFM analysis for the μ-casted electrode, j) the conventional electrode, and a comparison between the average roughness (R_a), root mean square roughness (R_q), and peak-to-peak height (R_t).

different classes (Class A = 140 μm, Class B = 210 μm, and Class C = 280 μm). The base height, the distance from the current collector to the surface of the base, was 70 μm, which was same for all three classes. However, the teeth heights, defined as the height from the surface of the base to the top surface of the 3D structure, were different in the different samples. These teeth heights were varied to change the mass loading and observe the SDP impact of higher mass electrodes on the battery performances. To achieve a higher teeth thickness compared to the base thickness, an initial casting was done at a base thickness of 20 μm and teeth thickness of 400 μm (for Class C sample, shown in Figure S5, Supporting Information). During drying process, the structure slightly collapsed and increased the base thickness (70 μm) and decreased the teeth thickness (210 μm). Therefore, after drying process the trapezoidal shaped structure was generated. In addition, the surface roughness of the electrode can be a critical part of the electrode performance as it can develop uneven current density and unwanted reactions. So, a more thorough look into the surface morphology of the electrodes can be seen in Figure 3d–g. The surface roughness of the base part (Figure 3d), the top part (Figure 3e), and the inclined edge (Figure 3f) of the patterned μ-casted electrode were similar throughout the entire electrode. Compared to the conventional structure shown in Figure 3g, the surface roughness was similar to the μ-casted electrode. To confirm the roughness, an atomic force microscopy (AFM) analysis was

conducted for both the μ-casted electrode (Figure 3i) and the conventional electrode (Figure 3j). From Figure 3k the average roughness (R_a) and root mean square roughness (R_q) was calculated as 0.12 and 0.15 μm for both electrodes, whereas the peak-to-peak height (R_t) for the conventional and the μ-casted electrode was 0.997 and 1.10 μm, respectively. Thus, there was no large difference in the surface roughness from the μ-casted electrode. Finally, the attachment, alignment and placement of the μ-casted electrodes and the separator were analyzed in Figure 3h, where the relatively smooth bending of the separator proved that the contact between the electrodes, current collectors, and the separator was sufficient.

2.3. Electrochemical Performance

First, to study the effect of SDP designed electrode structure in Class A (25 to 35 mg) samples on battery performance, the specific capacity and the areal capacity were investigated at a low C-rate of 0.1 C (**Figure 4**a). The specific capacity of the conventional planar electrodes (148 mAh g^{-1}) is relatively lower than the literature value (157 mAh g^{-1}), which is attributed to the high mass of the electrodes that were 2–3 times higher than the literature value,[23,25] where a higher electrode mass decreases the specific capacity. On the other hand, by using a 3D structured electrode, the capacity was comparable to the literature value despite its high mass.[23] It is also shown that the 3D architecture of the electrodes could achieve a greater specific capacity after cycling at 0.1 C for 200 cycles. In addition to the increased specific capacity, it was also found that the areal capacity for the 3D structured ultrathick electrode showed better performance than the conventional electrode structure. The previously reported discharge areal capacity for the conventional laminated NMC-811 electrode was 2.0 mAh cm^{-2} at 0.1 C after 20 cycles.[26] By increasing the mass of the electrode, the areal capacity for the conventional electrode also increased to 2.75 mAh cm^{-2} after 20 cycles at 0.1 C and maintained 2.9 mAh cm^{-2} at the 200th cycle. The impact of the higher C-rate was also compared with conventional and 3D electrodes (Figure 4b). Both the specific and areal capacity of the electrodes decreased due to the higher applied current, but the 3D electrodes showed 20–40% higher capacity over the conventional electrodes. Surprisingly, the SDP electrodes showed a higher areal capacity than the literature value[26] even after increasing the current five times higher. As shown in Figure 4c, the battery performance of both electrodes for C-rate performance was performed at 0.1 C, 0.2 C, 0.5 C, 1.0 C, and 0.1 C for 15 cycles each. All samples showed stable performance along with slight decreases in capacity. As expected, the capacity was reduced at high C-rates due to high ohmic resistance (detailed explanation is given in Section 2.5). The areal capacity of the 3D electrode battery (1.81 mAh cm^{-2}) was about 1.72 times that of the conventional electrode sample (1.05 mAh cm^{-2}) at 1 C. After returning to the low C-rate of 0.1 C, both cells showed stable performances, where the 3D electrodes (2.98 mAh cm^{-2}) showed 16% more areal capacity than the conventional electrodes (2.57 mAh cm^{-2}).

Next, as shown in Figure 4d–f,g–i, the conventional laminated electrode and the 3D electrode were compared by analyzing the specific capacity and areal capacity for Class B (35 to 45 mg) samples and Class C (45 to 55 mg), respectively. From Figure 4a,d,g, the higher mass of the electrodes reduced the specific capacity and enhanced the areal capacity. For instance, after the 20th cycle at 0.1 C (Figure 4a) the average specific capacity of Class A samples was 157.13 mAh g^{-1} for the 3D μ-casted electrodes and 144.90 mAh g^{-1} for the conventional electrodes, where for Class B samples (Figure 4d) the specific capacity was 155.67 mAh g^{-1} for the μ-casted electrodes and 136.33 mAh g^{-1} for the conventional electrodes. The higher mass loading reduced the specific capacity of the conventional electrode samples significantly, whereas the specific capacity of the μ-casted electrodes was not as pronouncedly decreased. Though the specific capacity was reduced with increased electrode mass, the areal capacity of the electrodes increased significantly at both 0.1 C and 0.5 C. The μ-casted Class C electrodes achieved a nearly doubled areal capacity over the conventional electrodes (Figure 4g,h), where the lower mass Class A electrodes showed an increase of 10% in areal capacity. Even after the 100th cycle, it was observed that the areal capacity of the Class B (3.01 mAh cm^{-2}) conventional electrodes increased by 14.6% from the Class A samples (2.57 mAh cm^{-2}), and for the μ-casted 3D electrodes the areal capacity increased by 23.6% after 100 cycles (3.77 mAh cm^{-2} for Class A and 3.05 mAh cm^{-2} for Class B). The enhanced capacity performance at different C-rates (0.1 C, 0.2 C, 0.5 C, 1.0 C, and 0.1 C for 15 cycles each) was also observed in Figure 4f. From Figure 4g,h, where a slight decrease in specific capacity occurred due to the very high mass (45–55 mg) of the Class C electrodes. At 0.1 C, a 4.69 mAh cm^{-2} areal capacity was achieved by the Class C electrode and at 0.5 C the areal capacity was 3.07 mAh cm^{-2}. From C-rate testing (Figure 4c,f,i), the difference between the capacity of the μ-casted 3D electrodes and the conventional laminated electrodes was more prominent with increasing C-rate and the difference was also expanded by increasing the electrode mass the of the μ-casted electrodes. In the high mass and thick conventional structured electrodes, the diffusion of ions is hindered because of the long diffusion path of the active material particles, caused by high-tortuosity and the far distance of the active particles from the interface of the electrodes. However, the 3D interdigitated electrodes with high mass can facilitate ionic diffusion because the structure, itself, allows for a reduced distance between the active particles and the interface of the electrodes, as shown in a later section. The capacity fade percentages were also higher in the conventional electrodes than the μ-casted 3D electrodes at 0.1 C and 0.5 C (Figure S2, Supporting Information). Increasing the mass of the electrodes also enhanced the specific capacity fade at high C-rate (Figure S2b, Supporting Information). More detailed results with the average, highest, and lowest values can be observed in Figure S4 of the Supporting Information.

By comparing the results for Class A and Class C (low mass and high mass, Figure 4a,g), it was observed that the specific capacity of the μ-casted electrode decreased ≈9% where the conventional laminated electrode decreased by 31%. In terms of the areal capacity there was a huge increase of 41% for the μ-casted electrode; on the other hand, the areal capacity of the conventional electrode only increased by ≈25% compared in Class A and Class C. Increasing the current rate to 1 C (Figure 4c,i) showed very promising performance in the μ-casted electrodes,

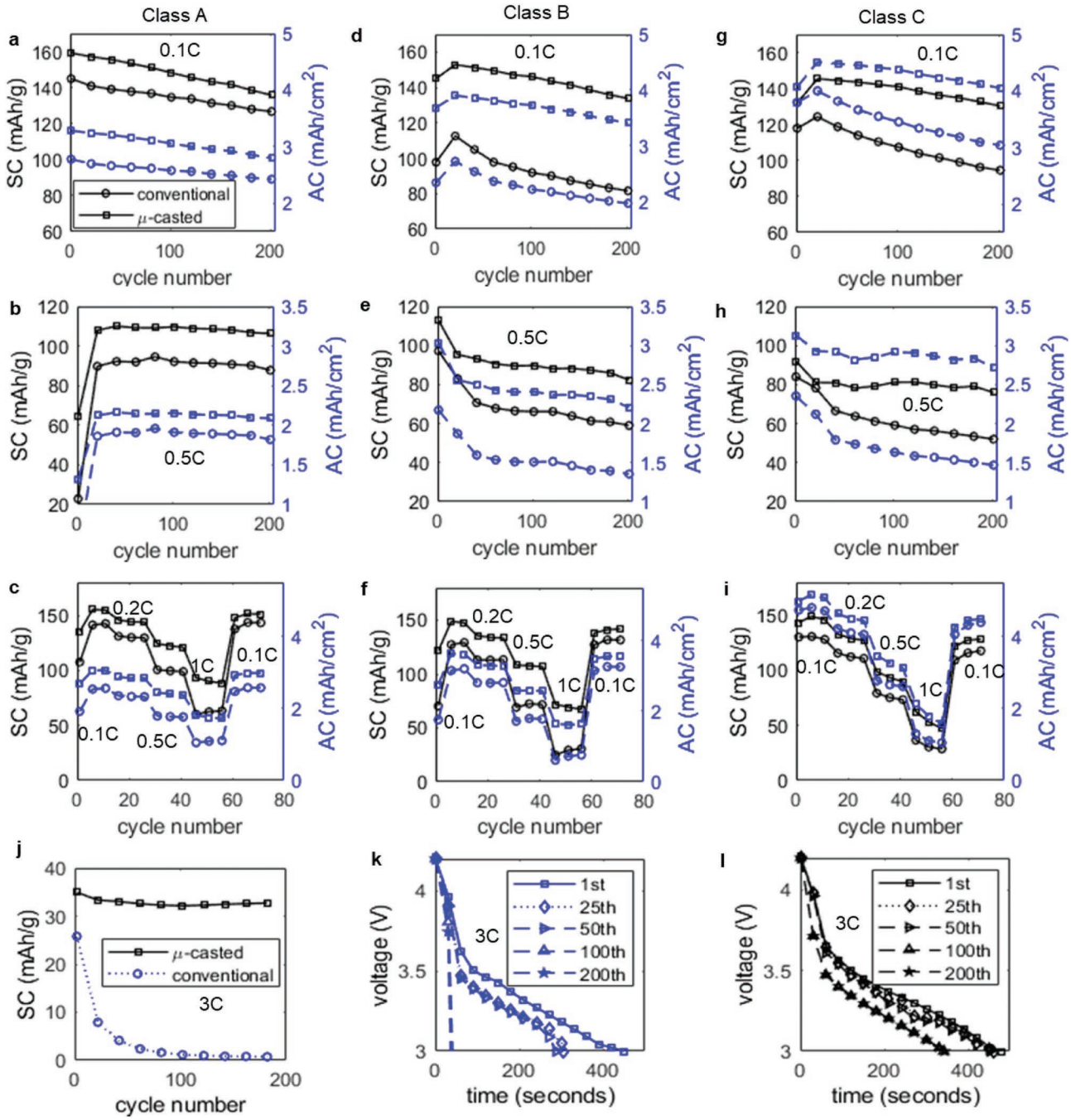

Figure 4. Specific capacity (SC) and areal capacity (AC) at 0.1 C, 0.5 C, and C-rate (0.1 C, 0.2 C, 0.5 C, 1 C, and 0.1 C) of a–c) the Class A samples: d–f) Class B samples, and g–i) Class C samples. Here dotted blue lines indicate AC and solid black lines indicate SC. j) Relative capacity comparison of the μ-casted and conventional batteries at 3 C for 200 cycles, and k) the voltage versus relative time for discharging in the 1st, 25th, and 50th cycles have been compared for μ-casted of Class C, and l) for the conventional casted of Class C.

where an 11.1% areal capacity increase was achieved compared to the conventional electrodes areal capacity that only increased by 1.5%. As expected, the reduction in specific capacity was higher at a high C-rate for both cases, where the μ-casted 3D structure still outperformed the conventional structure as the specific capacity reduced by 40% for μ-casted 3D structures and by 65% in the conventional electrodes. Increasing the current further to 3 C indicated that the Class C μ-casted electrodes could achieve significantly better rate capability over the Class C conventional electrodes, which suffered huge degradation in the relative capacity (Figure 4j). For the μ-casted sample the capacity retention was 93.59% after 200 cycles at 3 C where the conventional electrodes showed only 0.028% of capacity retention at 3 C after 200 cycles. Figure 4k,l shows the relative discharge time at different 1st, 25th, and 50th cycles for Class C samples where it can be clearly seen that faster degradation

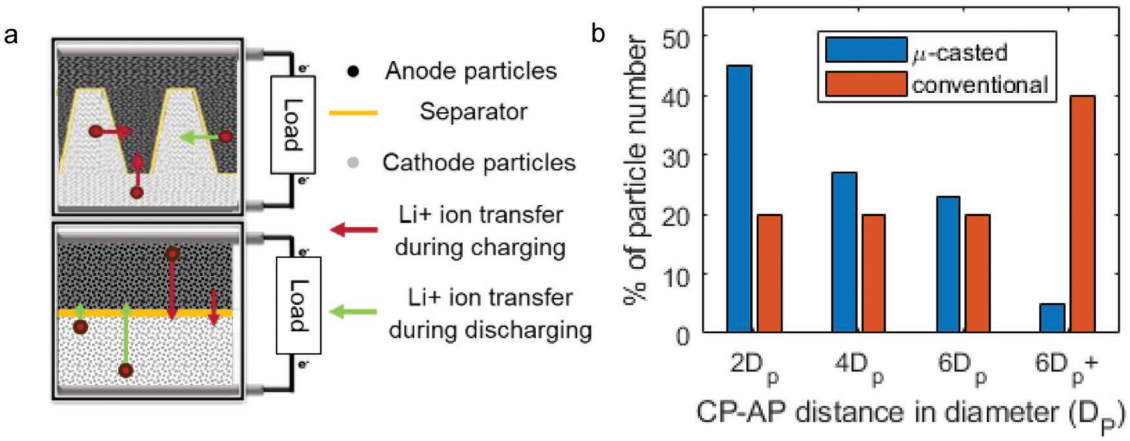

Figure 5. a) Particle distance among the particle in ultrathick electrode (arrows indicate the Li^+ ion movement), and b) bar chart showing the average distance between anode particle (AP) and cathode particle (CP) for SDP and LDP in μ-casted and conventional electrodes respectively, where D_p refers to the size of one particle which is ≈13 μm.

happened in the conventional thick electrode than the ultrathick μ-casted electrode. Furthermore, a comparison between recent works considering structured/interdigitated batteries[3,7,8,14,15] and the μ-casted battery was made in terms of areal capacity (Figure S7, Supporting Information). One of the main challenges of the thick electrode is to achieve good capacity retention and the LIBs could sustain less than 30 cycles in literature works.[3] Some of them mentioned about renewing the cathode after 20 cycles.[11,12] However, the μ-casted battery showed very high capacity retention after 20 cycles and also it could sustain more than 200 cycles. Another electrochemical energy density performance comparison has also been conducted in between the μ-casted and the conventional electrode (Figure S8, Supporting Information). Both the gravimetric and volumetric energy density were measured at different thickness of the electrode assembly (anode, cathode, separator, and current collectors). Higher gravimetric and volumetric energy density could be observed for the μ-casted structured batteries. In the μ-casted batteries, the trend of the gravimetric and volumetric energy density is increasing at higher thickness which refers to the SDP structural benefit for facile transportation of ions.

2.4. 3D Structures Reducing the Distance between Anode and Cathode Particles

The primary reason for the improvement found in the μ-casting process was the reduction in the ion diffusion path a result of the SDP interdigitated structure. The interparticle distance was compared between the 3D structured electrode and the conventional electrode. For this comparison, a small area of the electrodes with uniformly arranged particles were considered, with the 3D structure including two teeth and two bases (**Figure 5**a). Here Li^+ ions can transfer from one electrode to the other during charging and discharging, where the arrows show the diffusion path distance for transferring the Li^+ ion during charging and discharging. A shorter distance compared to conventional structures permits facile ion transference between the electrodes in the 3D structured ultrathick batteries. Conversely, a higher ion diffusion distance is unavoidable for the conventional electrodes, especially for the ions coming from the particles residing furthest from the electrode interface. To develop a clear understanding of the particle–particle distance from anode side to cathode, an analytical study was performed to compare the μ-casted and conventional electrode, in which perfectly spherical shaped active material particles with the same particle size and homogenous arrangement were considered for each structure, as shown in Figure S9 of the Supporting Information. The horizontal lengths of two teeth and two bases were near 260 μm (Class C) according to the SEM images (Figure 3a–c). For this evaluation, the geometries were considered with a particle size of 13 μm (according to Sigma-Aldrich) and the teeth thickness and gap size were maintained according to the SEM images shown in previous section. The average particle-to-particle distance measured form the cathode particles to the anode particles were evaluated, where for one cathode particle, the distance between that cathode particle and all the anode particles were measured first. It can be observed that in the μ-casted electrodes, most particles have a shorter distance to one another than in the conventional laminated structured electrodes. Specifically, 46% of the particles of the ultrathick 3D electrodes are in a distance within 0–26 μm from one another whereas only 20% of the particles of the conventional structured electrode are held in that range. Furthermore, most of the particles for the conventional electrode have a distance greater than 78 μm while only 5% of the particles of the μ-casted electrode are in that particle–particle distance range. On average, the Li^+ ions travel a shorter distance in the μ-casted batteries compared to the conventional case, which can be a reason for the performance improvement.

2.5. Impedance and Cyclic Voltammetry Analysis

Another important benefit of the μ-casted SDP electrode is its ability to facilitate Li^+ ion insertion and deinsertion between anode and cathode, which can be gauged by the electrode's impedance. An electrochemical impedance spectroscopy (EIS) analysis was conducted, where both the conventional laminated structured electrode and the μ-casted 3D structured electrode

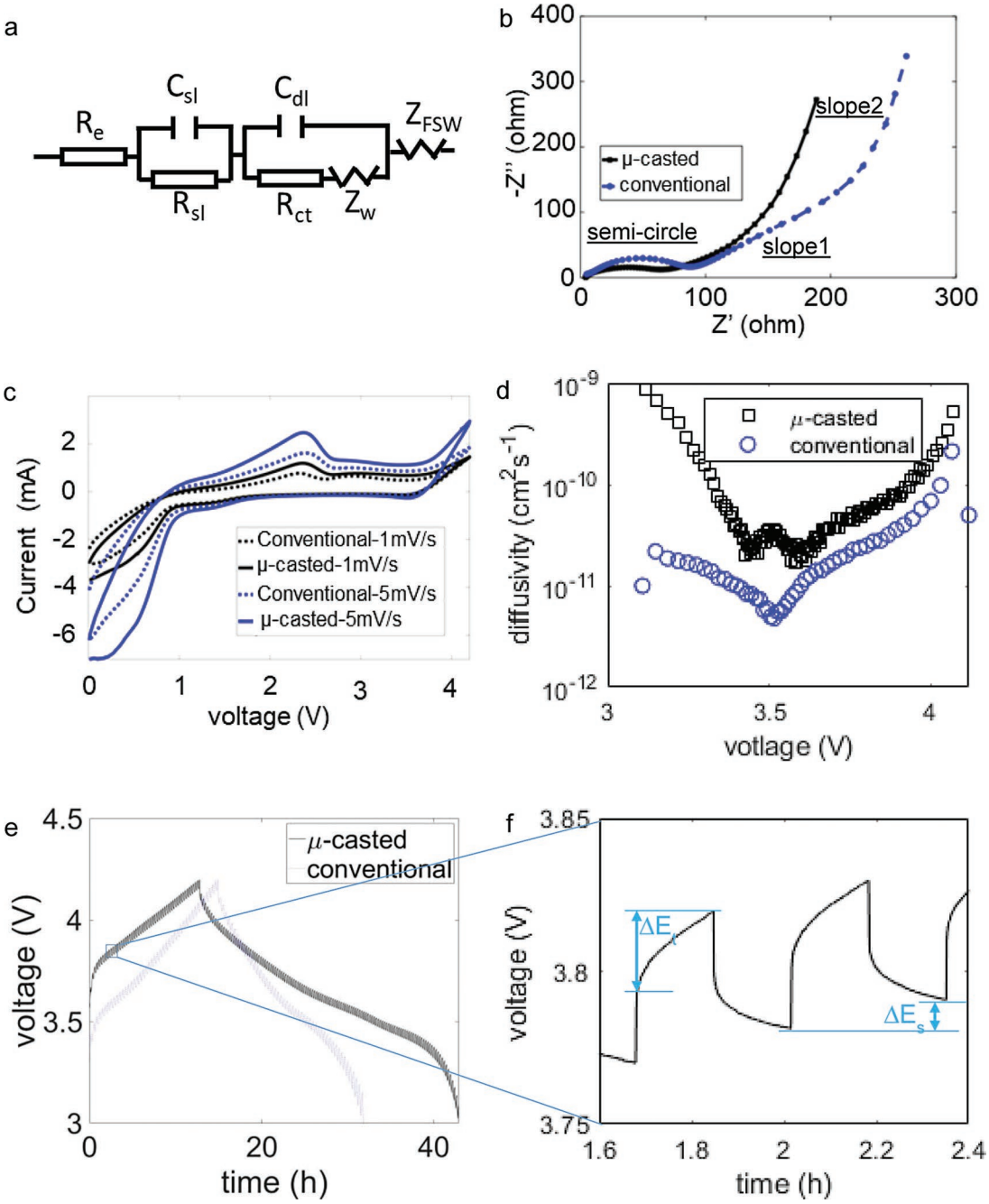

Figure 6. a) Circuit diagram for the Nyquist plot in EIS analysis. Comparison of the b) impedance with the conventional laminated structure and the 3D electrode structure, and c) voltage polarization in the 3D and conventional electrodes of NMC-811 by cyclic voltammograms 0.01 to 4.2 V, and scan rate impact on the samples. GITT test to observe the diffusivity at different voltage in the μ-casted electrodes and conventional electrodes d) where diffusivity is in logarithmic scale. e) The voltage profile of the electrodes where current was applied for 10 min and rested for 10 min for both charging and discharging and f) zoom-in voltage profile to show how the ΔE_s and ΔE_t were measured to calculated diffusivity.

were used from Class A samples. The Nyquist plots for the two samples were plotted in **Figure 6**a,b. The original data were fitted by using a circuit diagram model shown in Figure 6b.[27] Here, the high-frequency intercept at the Z' axis indicates the ohmic resistance, R_e, which is defined as the resistance of bulk electrolyte, and the semicircle in the middle-frequency range refers to the charge transfer resistance, R_{ct} and, C_{dl} (non-faradaic-branch consisting of the double layer capacitance), and R_{dl} are the double layer capacitance and resistance.[27] An interface with a surface layer was also considered by adding another R_{sl} (surface layer resistance) and C_{sl} (surface layer capacitance) component[27,28] Further, the Warburg impedance, Z_w, is referred to the synergetic effect of the diffusion of lithium ions on the electrode/electrolyte interfaces at semi-infinite length, which corresponds to the straight sloping line at low frequency.[29] In addition, finite space Warburg-type element

Z_{FSW} was used to describe the diffusion in a medium where the interface precludes the flow of the species and is represented by hyperbolic cotangent function.[27] Typically two semicircles can be observed in the Nyquist plot, the low-frequency semicircle indicates the charge transfer resistance R_{ct}[38] and the high frequency second semicircle relates to the kinetics of the electrochemical reaction, which can be impacted by surface coating, phase transition, bandgap structure, and particle size[37] and the long tail named Warburg tail is attributed to the diffusion of the ions.[27] Though the first semicircle (represented by R_{ct}, semicircle in Figure 6b) could be observed at low frequency, the second semicircle at high frequency could not be observed. This may be attributed to the dominant effect of the high diffusion of the ions, as two slopes (in the tail) are observed where the slope-1 is a converted semicircle at high frequency. Higher diffusion can also be indicated by the steepness of slope of the Warburg tail and the diffusion becomes challenging when it reaches near to 45° angle with the real impedance (Z') axis.[27] Both cells had a similar ohmic resistance (0.1 Ω), but the semicircle of the μ-casted 3D structure was smaller than that of the conventional laminated structure, where the R_{ct} of μ-casted 3D structure (65.24 Ω) was lower than that of the conventional laminated structure (88.41 Ω). As a result of low charge transfer resistance, more Li^+ ions can easily transfer in between the μ-casted anode and cathode than in the conventional laminated structured anode and cathode,[29,30] further providing a reason to why the μ-casted 3D structured electrode greatly enhanced the transport of lithium ions. From the EIS results, the Warburg tail (slope-2) of the conventional electrode is closer to 45° angle than μ-casted electrode and also the Warburg impedance (Z_w) of the μ-casted electrode was less than the impedance measured from the conventional laminated electrodes, which is directly related to the facile diffusion of the ions occurred due to the SDP structures. Observed values for the capacitance, resistance, and Warburg impedance are shown in Table S1 of the Supporting Information. To have better understanding about the diffusion, a galvanostatic intermittent titration technique (GITT) test was also conducted to observe the diffusivity (Figure 6d). The diffusion coefficients of the μ-casted and conventional batteries were measured using Equation (S1) of the Supporting Information.[45] More details of the experiment and diffusivity calculation can be found in the Experimental Section and in the Supporting Information. It was observed that the diffusion coefficient of the μ-casted battery was higher than the conventional battery.

The cyclic voltammetry (CV) curves (Figure 6c) for the μ-casted electrode and conventional electrode indicated that both samples had the same polarization value of around 2.3 V because the same cathode (NMC-811) and anode (MCMB) materials were used. Furthermore, the redox process was diffusion controlled, as opposed to adsorption controlled, as indicated by the peak current, which was proportional to the square root of the scan rate for both μ-casted and conventional electrodes at scan rates of 1 and 5 mV s^{-1}.[31] The results shown in Figure 6c are after the formation cycle, where the peaks generated correspond to the formation of an intermetallic components layer.[32] Both the 3D structure and the conventional structure yielded a similar peak (2.3 V) in the curve, as they had the same material composition and ratios as well as similar mass. The area under the CV curve for the μ-casted 3D structured electrode is larger than the conventional electrodes, which is caused by the shorter diffusion path in the ultrathick 3D electrodes.[32] The most prominent peaks (anodic and cathodic) were found in the CV test correspond to the literature, where pronounced peaks were located at those points.[31]

2.6. Mechanical Integrity

In the conventional thick cathode electrode, the components of the electrode are closely packed, which simultaneously creates a highly tortuous structure with low porosity and greatly inhibits battery performance as the cell is operated over a long period of time. To improve electrolyte permeability and the ion transfer rate, SDP designed porous structures are needed, where 3D architecture geometries have great utility in not only creating SDP electrode structures but also maintaining the structure over numerous cycles.[12] In this section, the impact of cycling on the electrode's tortuosity and defect formation was analyzed. Due to the continuous volume change that occurs with Li^+ ion (de)intercalation over long cycling and as well as a Li^+ ion concentration gradient that results in stress generation,[15] defect formation, and subsequent mechanical properties deterioration occur, which were investigated by observing both conventional and μ-casted electrode surfaces after cycling for 200 cycles as shown in **Figure 7**. This investigation was done at different locations on the electrode to observe both defects occurring locally as well as the defects formed on the total electrode surface. More images at different regions of the cycled electrodes are shown in Figure S3 of the Supporting Information to observe the overall generation of cracks and holes in the electrodes. The experimental observation of the cycled μ-casted cells did not show significant stress generation at the electrode level, which is shown later in the simulation-based study section. The 3D structured μ-casted electrode had less cracks, tortuous pores, and defects on the surface compared to the conventional laminated structure. Some void formation and tortuous pores generated on the surface of the μ-casted electrode surface were observed (Figure 7a), where the voids and cracks were deep and similar to the size of the one active material particle (13 μm) (Figure 7b). On the other hand, the degradation of the structure and surface property was more significant in the conventional structures than in the 3D structures (Figure 7c). Severe cracks, tortuous pores, and large fractures were found in the conventional electrode surface after 200 cycles (Figure 7c,d). In all electrodes, volume change occurs due to ion intercalation and deintercalation during cycling, which generates stress on the electrodes. With the 3D architecture, a shorter diffusion path can be achieved, which causes less changes in the concentration gradient and, therefore, volume change in the battery. Due to a lower change in the concentration gradient in the μ-casted electrode, it is possible to reduce the stress level on the ultrathick electrodes, whereas for the conventional structures it is not possible to reduce the stress development due to higher change in concentration gradient. This is the reason why the 3D architecture showed less defect formation during cycling compared to the conventional structure (as shown in Section 2.7). Furthermore, the delamination of the electrodes from the

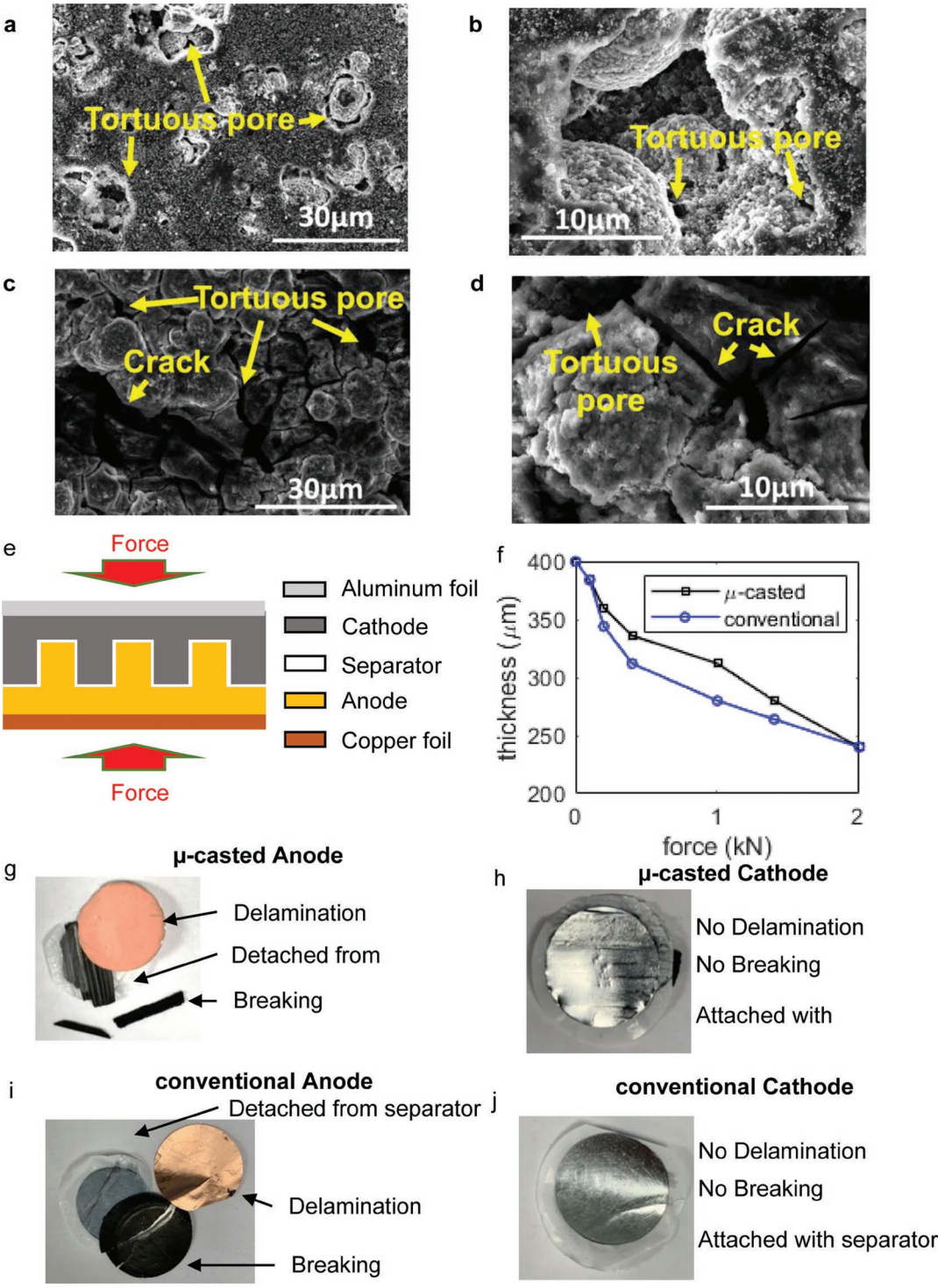

Figure 7. SEM images for deformation and defect analysis after 200th cycles of a,b) the 3D structured µ-casted electrode where some tortuous pores generated after cycling, and c,d) the conventional laminated electrode where large tortuous pores have been generated along with some large cracks formed. Mechanical properties analysis of the Class C µ-casted and conventional electrode assembly. The schematic diagram of the mechanical test setup where e) the biaxial compressive force was applied, f) the applied force decreases the total thickness, g) damaged anode after 4 kN applied force in µ-casted anode, and i) conventional anode, and cathode after applying 4 kN force in h) µ-casted cathode and j) conventional cathode.

current collector was not observed in either the µ-casted or conventional electrodes after 200 cycles, suggesting low stress generation as the delamination of the electrode from the current collector is directly related to the electrode level stress generation during long term cycling. Thus, the performance could be improved and maintained over numerous cycles and

could be attributed to the improvement in the mechanical stability imparted from the 3D structured μ-casted electrodes.

Another important consideration should be made about the mechanical stability of the μ-casted electrode. External loads can be developed during cell fabrication and also during mechanically extensive operations, where during the fabrication of cells the electrode may experience a load near 0.05 kN and in some extensive operation the value could be around 1.7 kN.[44] The mechanical properties of the assembly of anode, separator and cathode was analyzed where different compressive force was applied on the top and bottom of the assembly (Figure 7e). In this work, the applied load was considered from 0 to 2 kN to observe the impact of the force on the overall thickness of the assembly for Class C electrode sample. The thickness was decreasing when the force was increasing (Figure 7f). The result also compared with the conventional electrodes, which showed similar decreasing of thickness trend as the μ-casted showed however the μ-casted sample utilized the benefit of interdigitated structure and showed better mechanical stability than the conventional sample. Moreover, there was no delamination, breaking or detachment of the electrode from the separator up to 2 kN, however after applying 4 kN load, the anode (MCMB) was broken, delaminated, and also detached from the separator (Figure 7g,i) where the cathode (NMC-811) was not damaged even after 4 kN load (Figure 7h,j) for both the μ-casted sample and the conventional sample.

2.7. Stress Analysis Model

Any generated stresses may incur damage at both the particle level, which may take the form of particle pulverization and detachment, and the electrode level, which could consider electrode cracking and fracturing as well as hole formation. To investigate the stress generated in the 3D μ-casted electrodes and the conventional electrodes, a modeling study was conducted. The model was based on the porous electrode theory and the stress analysis was developed by considering electrochemical–mechanical interaction at the macroscale or electrode level and the microscale or particle level. First, the computational stress model has been validated with the experimental data by comparing the voltage profile in **Figure 8**a. It was observed that the experimental and simulation results align perfectly in terms of both the μ-casted and conventional electrodes. For the validation of the stress model, experimental results of the Class A electrodes were used.

The stress analysis was done after validating the model considering the stress generation at particle level and electrode level. At the particle level, the eigenstress can be alleviated by the μ-casted 3D structure (Figure 8b–g), where the largest eigenstress distributes on the electrode/electrolyte surface of the structure. This is because the Li^+ ion concentration change in these locations is highest, and the concentration change decides the eigenstress. At the macroscale, the stress in the conventional structure is negative, which indicates compression. In μ-casted 3D structure, the stretching occurs at the sides of teeth. The irregular change of particle stress is related to the geometry. Higher teeth could lead to a larger nonhomogeneity in Li^+ ion concentration since the diffusion path in teeth will become longer. Wider teeth could alleviate the concentration nonhomogeneity because it could increase the surface area in electrode, which is beneficial to charge transfer. Nonhomogeneity of Li^+ ion concentration is proportional to concentration change, as well as stress. In the geometry below, when the teeth height increase, the average width of the teeth also increases, which have a controversial effect with teeth height. Therefore, its impact is more complex, and the particle stress's change is not monotonous. Particle stress increased with the thickness increase in the conventional structure. It seems that in thicker samples, the average state of charge (SOC) at the end of discharge is higher, so that the SOC change is larger than in thin samples. Although the particle stress increases, a larger volume could also disperse the pressure. Therefore, the macroscale stress decreases as the thickness increases. The maximum tensile stress is distributed at the thinnest part of the structure and the thickness of the thinnest part of the μ-casted structures are same for all the classes. However, the curvature increases at the thinnest part as the teeth height increases, which results in a stress accumulation. Comparing the conventional structure and μ-casted 3D structure, although the maximum stress level is larger in μ-casted 3D structure with Class A, the average value of the stress magnitude is always larger in conventional structure. This is due to the larger change in the concentration gradient in the conventional electrode compared to the μ-casted electrode as the μ-casted 3D architecture allows a shorter diffusion path for the lithium ions. It is also observed that the higher massive μ-casted electrodes of Class C generate lower stress than the electrodes of Class A (Figure 8b–g). Due to the enhanced particle level stress generated in the conventional laminated structured electrode, more defects and deformations were found by experimental observation in Figure 7. The electrode level stress is small enough to not be of concern when considering the electrode level mechanical damage, such as delamination of electrode from the current collectors.

3. Conclusions

In this study, ultrathick electrodes were fabricated using a new μ-casting method, where a newly manufactured 3D doctor-blade is introduced, enabling efficient active materials usage and an SDP-designed 3D structure. The μ-casted electrodes achieved enhanced battery performance with both high areal and specific capacity by utilizing the advantages of high aspect ratio 3D structures to break through the performance tradeoffs posed by the conventional laminated structure. Moreover, these μ-casted electrodes can be applied to large scale battery formats, which resolves the challenges of time-consuming and costly process in traditional 3D battery manufacturing technologies. A significant enhancement in capacity of the battery has been achieved by this μ-casted SDP 3D structured electrodes. Though the mass of the electrodes is more than 2.5 times higher than the usual electrode mass for coin cells, the 3D structured NMC-811 battery shows very good performance in terms of both specific capacity and areal capacity (159.4 mAh g^{-1} and 3.51 mAh cm^{-2}) with a good cycle life. For the high mass 3D electrodes (5–6 times the mass of conventional electrodes), the specific capacity was reduced only by 11% and the areal capacity improved by 32.5%.

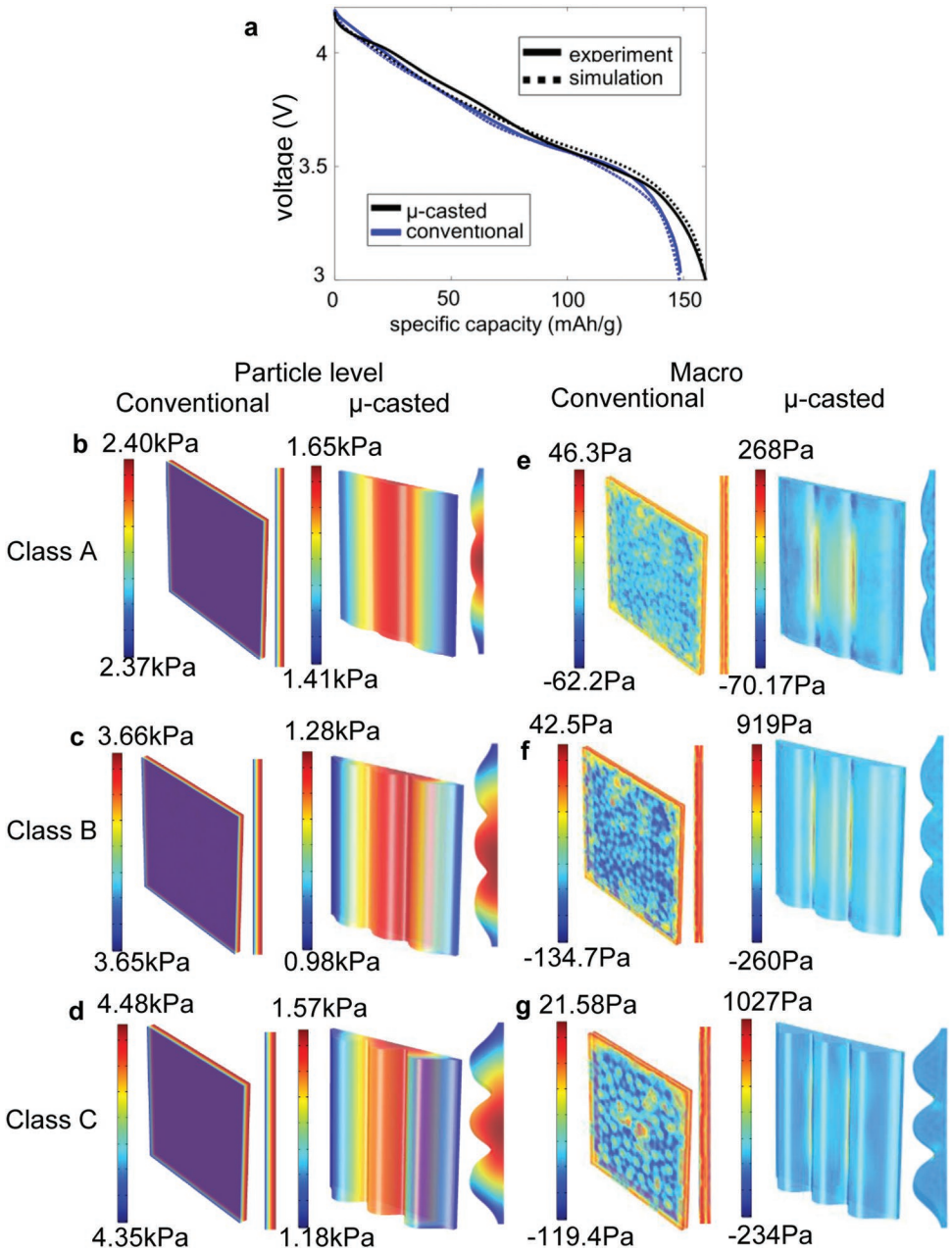

Figure 8. a) Validation of the stress model by considering the voltage profile. Maximum tensile stress distribution modeling results comparing the conventional laminated structure and the 3D μ-casted structure with b–d) particle level and e–g) macrolevel analysis of Class A (b,e), Class B (c,f), and Class C (d,g), where the negative sign indicates compression.

These results indicate that compared to the conventional electrodes, the μ-casted SDP electrodes were more efficient and had much higher lithium ions transport, which presents a new possibility for preparing an ultrathick electrode with excellent electrochemical performance. This work introduces a simple and convenient route for the fabrication of 3D ultrathick electrodes using the traditional separator materials and assembly issues, which can be used for a scaled-up 3D battery manufacturing process via the tape casting method. By improving the automation and industrial technique this process can be faster and the production rate could be similar to the production rate for the currently used method in the battery industries. It was also observed that the μ-casted structures provide a high interface area and short diffusion path for the ion movement, which is of critical importance as ions transfer between the electrode and the electrolyte interfaces. Another aspect of the μ-casted structures is that there is no fundamental barrier for implementation into a stacked cell, which is a popular method to prepare commercial batteries. Based on these results, it is believed that this casting 3D electrode technique will find its widespread applications in the low-cost, large-scale, and roll-to-roll compatible manufacturing of next generation 3D batteries.

4. Experimental Section

Materials and Paste Preparation: In this work, a $LiNi_{0.8}Co_{0.10}Mn_{0.10}O_2$ (NMC-811) paste was used to fabricate the cathode and MCMB was used to fabricate the anode. The cathode pastes were prepared by combining 85.5 wt% NMC-811 powder (Linyi Gelon LIB Co. Ltd., 13 µm) with conductive agent 6.5 wt% carbon black (CB, Alfa Aesar) and 8 wt% polyvinylidene fluoride (PvdF, Sigma-Aldrich) binder, and then dissolved in *N*-methyl-2-pyrrolidone solvent (NMP, Sigma-Aldrich). The anode pastes were prepared by mixing 85 wt% MCMB powder (MTI corp., 17.65 µm) with 5 wt% CB (Alfa Aesar) and 10 wt% PvdF and dispersed in NMP. The pastes were mixed by using a Speed Mixer (Flack Teck Inc.) at 3500 rpm for 20 min at room temperature.

Porosity and Thickness Measurement: The pastes were prepared with solvent (NMP) and the solvents were evaporated during the drying process. To measure the porosity, first the mass and the volume of the electrodes were measured by using weight balance and digital calipers. Digital calipers were also used to measure the thickness of the assembly. If the thickness of the assembly was greater than the calculated assembly thickness, it would be a misalignment between the electrodes (Figure S11, Supporting Information).

The density of the materials used in paste making are known from the materials specification sheets provided by the vendors. The volume was calculated by using the measured mass, density, and composition of the paste and the actual volume was measured using the calipers. The porosity was then calculated from the measured volume and the calculated volume.

Electrode Fabrication and Cell Assembly and Test: A newly designed doctor blade (Figure 1a) was developed and used for manufacturing ultrathick µ-casted 3D electrodes to obtain high-capacity lithium-ion battery. The new 3D doctor blade material was stainless steel and manufactured by using an EDM (SODICK, model- LN2W) wire system. The EDM can cut according to the design CAD file, where the wire moves to create high friction. This frictional force can cut the stainless-steel metal into the desired designed shape. In the 3D doctor blade, the teeth length was 0.2 mm, and the base length was 0.6 mm. From the experiment, it was observed that after evaporating the solvents from the paste the structure shrank by three times. In order to maintain equal gap and teeth size the doctor blade teeth and base length was in a ratio of 1:3. Aluminum foil (12.5 µm thick) was used as the substrate for casting and as a current collector for the cathode (Figure 1b). The electrode paste was casted by the conventional doctor blade, followed by the 3D doctor blade to create the thick µ-casted 3D structured design. For casting the anode materials, copper foil (10 µm thick) was used as the casting substrate and as the current collector. After casting, the electrodes were dried by heating at 120 °C for 6.5 h over a hotplate, where traditionally made electrodes were usually dried for overnight.[12] This type of µ-casted 3D structured electrode made via extrusion-based 3D printing typically takes ≈2.5 h to make 100 cm^2 areal electrode.[14,15] whereas by utilizing the 3D doctor blade it takes only 30 min to fabricate 100 cm^2 areal 3D electrode (Figure S1, Supporting Information). Afterward, the electrodes were cut to fit within a CR 2032 coin cell casing (Wellcos Corp.), where the diameters of the cathode and anode electrodes were 14 and 16 mm, respectively. The cathodes were prepared with 16.24 to 35.72 mg cm^{-2} for Class A to Class C samples.

The coin cell assembly was done inside a moisture and oxygen-controlled argon-filled glove box (MBRAUN). A 25 µm commercial PP/PE/PP (polypropylene/polyethylene/polypropylene) membrane (Celgard) was used as the separator and 0.5 mL of the electrolyte 1 M $LiFP_6$ (lithium hexafurophosphate) in EC:DMC (ethylene carbonate:dimethyl carbonate) 1:1 (Sigma-Aldrich) was used. The cell components, electrodes, and separator were sequentially placed inside the coin cell as shown in Figure 1b. To ensure the alignment of the structures, the thickness of the anode, separator, and cathode was individually measured before careful assembly and the thickness of the final assembly was checked. If the alignment was not correct, then the thickness of the assembly would be higher than the sum of the thickness of each component. By checking the total thickness of anode, separator, and cathode when assembled together, the alignment issue was solved. The paste characteristics were measured by a viscometer (Brookfield model HB) equipped with CAP-52Z cone spindle. The electrochemical behavior of the assembled batteries was measured by using a battery testing station (NEWARE) at a voltage range between 3 and 4.2 V according to the recommended values from the raw materials vendor. The specific capacity and areal capacity were measured at different current densities to observe the performance under different current loads. Potentiostatic battery impedance was also measured at a frequency range of 10 mHz to 5 MHz at a sinusoidal amplitude of 10 mV via EIS using a potentiostat (IVIUM STAT, Ivium Tech) and cyclic voltammetry was done at different scan rates at a voltage window of 0 to 4.2 V. All the fabricated structures were examined via SEM (Hitachi S4700). The surface roughness was measured through AFM by a NanoMagnetics Instruments ezAFM atomic force microscope. GITT test was done using NEWARE battery tester at a voltage range of 4.2 V for charging and 3 V for discharging where all the charging steps were for 10 min and a resting time for each step was 10 min. For GITT measurement, all the cells were from Class A to compare the diffusion coefficient. The charging and discharging current were 0.1 C for GITT. The diffusion coefficient was calculated according to Equation (S1) of the Supporting Information.[45] The mechanical properties were evaluated by using a hydraulic press (Strongway). First the anode, cathode, and separators were assembled together, and then different loads (0 to 4 kN) were applied from top and bottom of the assembly (Figure 7e). The thickness of the assembly was measured by a digital caliper. The initial thickness (at load = 0 kN) was measured before applying any load.

Modeling for Stress Analysis: The stress generation in the electrodes was evaluated by using a 3D electrochemical–mechanical model, which is based on the theory of porous electrode. For the modeling, first a sketch of the electrode is designed as geometry and meshed according to finite element method. The relevant equations of electrochemical behavior were reported in the previous papers.[20,33,36] In order to evaluate the stress generation in the electrodes, a model using the electrochemical–mechanical interaction at macro- and microscales was developed. The microscale stress model considered the stress generated inside the particle induced by Li^+ ion concentration changes and the macroscale stress model considered the stress generated across the entire electrode structure caused by the volume change of individual particles.

The radial stress, σ_r, and tangential stress, σ_t, of individual particle can be expressed as[34]

$$\sigma_r = \frac{2\Omega E}{3(1-\nu)}\left(\frac{1}{r_0^3}\int_0^{\tau_0} C_{s,avg} r^2\,dr - \frac{1}{r^3}\int_0^{r} C_{s,avg} r^2\,dr\right) \tag{1}$$

$$\sigma_t = \frac{\Omega E}{3(1-\nu)}\left(\frac{2}{r_0^3}\int_0^{\tau_0} C_{s,avg} r^2\,dr + \frac{1}{r^3}\int_0^{r} C_{s,avg} r^2\,dr - C_{s,avg}\right) \tag{2}$$

where r_0 is the radius of the particle, E is effective Young's modulus (considering porosity), ν is Poisson ratio, and Ω is the partial molar volume expansion of active material.

The boundary condition at particle surface ($r = r_0$) is set as

$$e_s^{ch} = \frac{1}{3}\left(\frac{(r_0 + u_{surf})^3}{r_0^3} - 1\right); \sigma_t = \frac{\Omega E}{3(1-\nu)}\left(C_{s,avg} - C_{s,surf}\right) \tag{3}$$

The tangential stress–strain relations and strain–displacement relations can be expressed as

$$\varepsilon_t = \frac{1}{E}(\sigma_t - \nu(\sigma_r + \sigma_t)) + \frac{\Omega}{3} C_{s,avg} \tag{4}$$

$$\varepsilon_t = \frac{u}{r} \tag{5}$$

Therefore, the particle surface displacement can be calculated as

$$u_{surf} = \frac{\Omega r_0}{3}(C_{s,avg} - C_0) \tag{6}$$

The microscale chemically induced eigenstrain e^{ch} is equal to the particles' volumetric strain in spherical particles, which is

$$e_s^{ch} = \frac{1}{3}\left(\frac{(r_0 + u_{surf})^3}{r_0^3} - 1\right) \tag{7}$$

According to the Mori–Tanaka effective-field theory, the macroscale eigenstrain e^{ch} can be computed as[35]

$$e^{ch} = e_m^{ch} + \varepsilon_s(e_s^{ch} - e_m^{ch}) + \varepsilon_s(C_s^{-1} - C_m^{-1})b_s \tag{8}$$

where ε_s is solid phase volume fraction, and e_m^{ch} is the chemically induced strain in the electrolyte, which is assumed to be 0 here. C_s and C_m are the stiffness matrices for the solid and liquid phase, while b_s is a function of both stiffness matrix. The governing equation of macroscale mechanical deformation is

$$\Delta \cdot \sigma = 0 \tag{9}$$

$$\sigma = C_{eff} : (e - e_{ch});\ e = 1/2(\Delta u + \Delta u^T) \tag{10}$$

where σ is the macroscale stress, e is the total macroscale strain tensor, and u is the total displacement, and C_{eff} is the effective elasticity tensor can be calculated as

$$C_{eff} = C_m + \varepsilon_s(C_s - C_m)A_s \tag{11}$$

$$A_s = A_D[(1 - \varepsilon_s)I + \varepsilon_s A_D]^{-1} \tag{12}$$

$$A_D = [(I + SC_m^{-1}(C_s - C_m]^{-1} \tag{13}$$

where S is Eshelby's tensor, which is a function of the aspect ratio of the particle and the Poison's ratio of the matrix phase.

Supporting Information

Supporting Information is available from the Wiley Online Library or from the author.

Acknowledgements

The authors gratefully acknowledge financial support from the National Science Foundation (CMMI 1917055).

Conflict of Interest

The authors declare no conflict of interest.

Data Availability Statement

The data that support the findings of this study are available in the supplementary material of this article.

Keywords

electrode architectures, electrode structure engineering, ion-transfer kinetics, short diffusion path design, thick electrodes

Received: April 20, 2022
Revised: June 19, 2022
Published online: July 19, 2022

[1] T. S. Arthur, D. J. Bates, N. Cirigliano, D. C. Johnson, P. Malati, J. M. Mosby, E. Perre, M. T. Rawls, A. L. Prieto, B. Dunn, *MRS Bull.* **2011**, *36*, 523.
[2] R. J. Brodd, *Batteries for Sustainability*, Springer, New York, NY **2013**, pp. 1–4.
[3] L. Lu, X. Han, J. Li, J. Hua, M. Ouyang, *J. Power Sources* **2013**, *226*, 272.
[4] N. Nitta, F. Wu, J. T. Lee, G. Yushin, *Mater. Today* **2015**, *18*, 252.
[5] K. G. Gallagher, S. E. Trask, C. Bauer, T. Woehrle, S. F. Lux, M. Tschech, P. Lamp, B. J. Polzin, S. Ha, B. Long, Q. Wu, W. Lu, D. W. Dees, A. N. Jansen, *J. Electrochem. Soc.* **2015**, *163*, A138.
[6] J. Park, J. Li, W. Lu, A. M. Sastry, *J. Appl. Phys.* **2016**, *119*, 025101.
[7] J. W. Long, B. Dunn, D. R. Rolison, H. S. White, *Chem. Rev.* **2004**, *104*, 4463.
[8] S. Ferrari, M. Loveridge, S. D. Beattie, M. Jahn, R. J. Dashwood, R. Bhagat, *J. Power Sources* **2015**, *286*, 25.
[9] W. Pfleging, J. Pröll, *J. Mater. Chem. A* **2014**, *2*, 14918.
[10] a) S. R. Gowda, A. Leela Mohana Reddy, X. Zhan, H. R. Jafry, P. M. Ajayan, *Nano Lett.* **2012**, *12*, 1198; b) J. B. Bates, N. J. Dudney, B. Neudecker, A. Ueda, C. D. Evans, *Solid State Ionics* **2000**, *135*, 33.
[11] a) N. Li, C. R. Martin, *J. Electrochem. Soc.* **2001**, *148*, A164; b) S. Yang, C. Zhou, Q. Wang, B. Chen, Y. Zhao, B. Guo, Z. Zhang, X. Gao, R. Chowdhury, H. Wang, C. Lai, N. P. Brandon, B. Wu, X. Liu, *Energy Environ. Mater.* **2021**, 1.
[12] a) Y. Kuang, C. Chen, D. Kirsch, L. Hu, *Adv. Energy Mater.* **2019**, *9*, 1901457; b) C. Huang, C. L. A. Leung, P. Leung, P. S. Grant, *Adv. Energy Mater.* **2021**, *11*, 2002387.
[13] M. Singh, J. Kaiser, H. Hahn, *J. Electrochem. Soc.* **2015**, *162*, A1196.
[14] a) J. Li, M. C. Leu, R. Panat, J. Park, *Mater. Des.* **2017**, *119*, 417; b) J. Li, X. Liang, R. Panat, J. Park, *ECS Trans.* **2018**, *85*, 369.
[15] J. Li, X. Liang, F. Liou, J. Park, *Sci. Rep.* **2018**, *8*, 1846.
[16] X. Tang, B. Lin, Y. Ge, Y. Ge, C. Lu, S. V. Savilov, S. M. Aldoshin, H. Xia, *Mater. Res. Bull.* **2015**, *69*, 2.
[17] K. Sun, T.-S. Wei, B. Y. Ahn, J. Y. Seo, S. J. Dillon, J. A. Lewis, *Adv. Mater.* **2013**, *25*, 4539.
[18] a) I. Gibson, D. Rosen, B. Stucker, *Additive Manufacturing Technologies*, Springer, New York, NY **2015**, pp. 399–435; b) J. J. Adams, E. B. Duoss, T. F. Malkowski, M. J. Motala, B. Y. Ahn, R. G. Nuzzo, J. T. Bernhard, J. A. Lewis, *Adv. Mater.* **2011**, *23*, 1335; c) E. Feilden, E. G.-T. Blanca, F. Giuliani, E. Saiz, L. Vandeperre, *J. Eur. Ceram. Soc.* **2016**, *36*, 2525; d) W. Li, A. Ghazanfari, M. C. Leu, R. G. Landers, *Virtual Phys. Prototyping* **2017**, *12*, 193; e) B. Y. Ahn, E. B. Duoss, M. J. Motala, X. Guo, S.-I. Park, Y. Xiong, J. Yoon, R. G. Nuzzo, J. A. Rogers, J. A. Lewis, *Science* **2009**, *323*, 1590; f) A. M. Gaikwad, G. L. Whiting, D. A. Steingart, A. C. Arias, *Adv. Mater.* **2011**, *23*, 3251.
[19] M. S. Saleh, J. Li, J. Park, R. Panat, *Addit. Manuf.* **2018**, *23*, 70.
[20] a) Y. Zhu, J. Li, M. S. Saleh, H. Pham, T. P. Plateau, R. Panat, J. Park, *J. Power Sources* **2020**, *476*, 228593; b) J. Park, J. Li (University of Missouri System), *U.S. Patent 10804524*, **2020**.
[21] L. J. Deiner, T. L. Reitz, *Adv. Eng. Mater.* **2017**, *19*, 1600878.
[22] a) D. S. Engstrom, B. Porter, M. Pacios, H. Bhaskaran, *J. Mater. Res.* **2014**, *29*, 1792; b) K. Fu, Y. Wang, C. Yan, Y. Yao, Y. Chen, J. Dai, S. Lacey, Y. Wang, J. Wan, T. Li, Z. Wang, Y. Xu, L. Hu, *Adv. Mater.* **2016**, *28*, 2587; c) S.-H. Kim, K.-H. Choi, S.-J. Cho, S. Choi, S. Park,

S.-Y. Lee, *Nano Lett.* **2015**, *15*, 5168; d) M. Nathan, D. Golodnitsky, V. Yufit, E. Strauss, T. Ripenbein, I. Shechtman, S. Menkin, E. Peled, *J. Microelectromech. Syst.* **2005**, *14*, 879; e) H.-S. Min, B. Y. Park, L. Taherabadi, C. Wang, Y. Yeh, R. Zaouk, M. J. Madou, B. Dunn, *J. Power Sources* **2008**, *178*, 795; f) H. Mazor, D. Golodnitsky, L. Burstein, A. Gladkich, E. Peled, *J. Power Sources* **2012**, *198*, 264; g) K. Heungsoo, J. Proell, R. Kohler, W. Pfleging, A. Pique, *J. Laser Micro/Nanoeng.* **2012**, 101; h) K. Yoshima, H. Munakata, K. Kanamura, *J. Power Sources* **2012**, *208*, 404; i) J. H. Pikul, H. Gang Zhang, J. Cho, P. V. Braun, W. P. King, *Nat. Commun.* **2013**, *4*, 1732.

[23] M. N. AL-Shroofy, Ph.D. Theses, University of Kentucky **2017**, pp. 1–100.

[24] a) S. K. Cheah, E. Perre, M. Rooth, M. Fondell, A. Hårsta, L. Nyholm, M. Boman, T. Gustafsson, J. Lu, P. Simon, *Nano Lett.* **2009**, *9*, 3230; b) M. M. Shaijumon, E. Perre, B. Daffos, P. L. Taberna, J. M. Tarascon, P. Simon, *Adv. Mater.* **2010**, *22*, 4978; c) J. W. Long, *Acc. Chem. Res.* **2007**, *40*, 854; d) H. Habazaki, M. Kiriu, H. Konno, *Electrochem. Commun.* **2006**, *8*, 1275.

[25] K. G. Gallagher, S. E. Trask, C. Bauer, T. Woehrle, S. F. Lux, M. Tschech, P. Lamp, B. J. Polzin, S. Ha, B. Long, *J. Electrochem. Soc.* **2015**, *163*, A138.

[26] L. Chen, X. Fan, X. Ji, J. Chen, S. Hou, C. Wang, *Joule* **2019**, *3*, 732.

[27] M. Mohamedi, D. Takahashi, T. Uchiyama, T. Itoh, M. Nishizawa, I. Uchida, *J. Power Sources* **2001**, *93*, 93.

[28] D. Guo, Z. Chang, H. Tang, B. Li, X. Xu, X.-Z. Yuan, H. Wang, *Electrochim. Acta* **2014**, *123*, 254.

[29] S. S. Zhang, K. Xu, T. R. Jow, *Electrochim. Acta* **2006**, *51*, 1636.

[30] a) Q.-C. Zhuang, T. Wei, L.-L. Du, Y.-L. Cui, L. Fang, S.-G. Sun, *J. Phys. Chem. C* **2010**, *114*, 8614; b) S. Cho, C.-F. Chen, P. P. Mukherjee, *J. Electrochem. Soc.* **2015**, *162*, A1202.

[31] a) X. Li, K. Zhang, M. Wang, Y. Liu, M. Qu, W. Zhao, J. Zheng, *Sustainable Energy Fuels* **2018**, *2*, 413; b) N. Elgrishi, K. J. Rountree, B. D. McCarthy, E. S. Rountree, T. T. Eisenhart, J. L. Dempsey, *J. Chem. Educ.* **2018**, *95*, 197.

[32] R. R. Salunkhe, K. Jang, H. Yu, S. Yu, T. Ganesh, S.-H. Han, H. Ahn, *J. Alloys Compd.* **2011**, *509*, 6677.

[33] J. Li, X. Liang, R. Panat, J. Park, *J. Electrochem. Soc.* **2018**, *165*, A3566.

[34] X. Zhang, W. Shyy, A. M. Sastry, *J. Electrochem. Soc.* **2007**, *154*, A910.

[35] S. Golmon, K. Maute, M. L. Dunn, *Comput. Struct.* **2009**, *87*, 1567.

[36] Y. Zhu, T. Plateau, B. Riemann, R. Landers, J. Park, *IFAC-PapersOnLine* **2021**, *54*, 374.

[37] N. Laszczynski, S. Solchenbach, H. A. Gasteiger, B. L. Lucht, *J. Electrochem. Soc.* **2019**, *166*, A1853.

[38] M. Gaberšček, *Nat. Commun.* **2021**, *12*, 6513.

[39] Y. Zhang, Y. Katayama, R. Tatara, L. Giordano, Y. Yu, F. Yang, J. Sun, M. J. Guangwe, R. Jung, M. Z. Bazant, Y. Shao-Horn, *Energy Environ. Sci.* **2020**, *13*, 183.

[40] E. N. Primo, M. Chouchane, M. Touzin, P. Vazquez, A. A. Franco, *J. Power Sources* **2021**, *488*, 229361.

[41] J. Chen, J. Liu, Y. Qi, T. Sun, X. Li, *J. Electrochem. Soc.* **2013**, *160*, A1502.

[42] S. Choi, T.-H. Kim, J. Lee, J. Kim, H.-K. Song, S. Park, *ChemSusChem* **2014**, *7*, 3483.

[43] M. Singh, J. Kaiser, H. Hahn, *Batteries* **2016**, *2*, 35.

[44] H. H. Heimes, C. Offermanns, A. Mohsseni, H. Laufen, U. Westerhoff, L. Hoffmann, P. Niehoff, M. Kurrat, M. Winter, A. Kampke, *Energy Technol.* **2020**, *8*, 1900118.

[45] W. Weppner, R. A. Huggins, *J. Electrochem. Soc.* **1977**, *124*, 1569.